SUPPORTING INFORMATION

Structural anisotropy of cyanido-bridged $\{Co^{II}_9W^{V}_6\}$ Single-Molecule Magnets induced by bidentate ligands: towards the rational enhancement of energy barrier

Szymon Chorazy,[a,b] Michał Rams,[c] Anna Hoczek,[a] Bernard Czarnecki,[a] Barbara Sieklucka,[a] Shin-ichi Ohkoshi*[b], and Robert Podgajny*[a]

[a]*Faculty of Chemistry, Jagiellonian University, Ingardena 3, 30-060 Kraków, Poland. E-mail: robert.podgajny@uj.edu.pl*
[b]*Department of Chemistry, School of Science, The University of Tokyo, 7-3-1 Hongo, Bunkyo-ku, 113-0033 Tokyo, Japan. E-mail: ohkoshi@chem.s.u-tokyo.ac.jp* [c]*Institute of Physics, Jagiellonian University, Łojasiewicza 11, 30-348 Krakow, Poland.*

Experimental details

Materials

$Na_3[W^V(CN)_8]\cdot 4H_2O$ precursor was synthesized according to the published procedures.[S1-S2] $Co^{II}Cl_2\cdot 6H_2O$ (Sigma-Aldrich, CAS: 7791-13-1), 2,2'-bipyridine-N,N'-dioxide (Sigma-Aldrich, CAS: 7275-43-6), and the solvents were purchased from commercial sources, reagent grade, and used without purification.

Synthesis and basic characterization of 1

The 0.06 mmol (14.3 mg) portion of $Co^{II}Cl_2\cdot 6H_2O$, and the 0.04 mmol (21.3 mg) portion of $Na_3[W^V(CN)_8]\cdot 2H_2O$ were dissolved together in the 4 mL of a methanol – acetonitrile (MeOH–MeCN, 1:1, v/v) mixture. Then, the freshly prepared solution of 2,2'-bipyridine-N,N'-dioxide (2,2'-bpdo, 0.06 mmol, 11.3 mg) in the 2 mL of a methanol – acetonitrile (1:1, v/v) mixture was carefully added. The resulting dark red solution often contained a small amount of brown precipitate which was removed by filtration. The clear solution was then put to a water bath with the temperature of 30 °C. After several days of crystallization, the large amount of dark red block crystals of **1** appeared.

The crystalline sample of **1** was identified as $\{Co^{II}[Co^{II}(2,2'\text{-bpdo})(MeOH)]_7[Co^{II}(MeOH)_3][W^V(CN)_8]_6\}\cdot\{Co^{II}[Co^{II}(2,2'\text{-bpdo})(MeOH)]_6[Co^{II}(MeOH)_3]_2[W^V(CN)_8]_6\}\cdot 8H_2O\cdot 2MeCN\cdot 27MeOH$ by the single-crystal X-ray diffraction study. While washed with MeOH and exposed to the air, they exchange relatively quickly MeOH and MeCN molecules to H_2O molecules to reach a general composition $\{Co^{II}_{18}(2,2'\text{-bpdo})_{13}[W^V(CN)_8]_{12}\}\cdot 36H_2O$ (**1**$^{\mathbf{hyd}}$) which presumably correspond to the phase with two different clusters identified as $\{Co^{II}[Co^{II}(2,2'\text{-bpdo})(H_2O)]_6[Co^{II}(H_2O)_3]_2[W^V(CN)_8]_6\}\cdot\{Co^{II}[Co^{II}(2,2'\text{-bpdo})(H_2O)]_7[Co^{II}(H_2O)_3][W^V(CN)_8]_6\}\cdot 50H_2O$. The preservation of the W^V oxidation state in **1**$^{\mathbf{hyd}}$ was checked by IR spectroscopy (Figure S1) while the amount of water and 2,2'-bpdo ligands were found from the CHN elemental analysis supported by the results of thermogravimetric measurement (Figure S2). Yield calculated using the obtained mass of **1**$^{\mathbf{hyd}}$: 19.5 mg, 61.5 %.

IR (KBr, cm^{-1}, Figure S1). CN^- stretching vibrations: 2181m, 2153m, indicated the presence of $[W^V(CN)_8]^{3-}$ ions.[S3] Other peaks: 3390vs,br, O-H hydrogen bonding; 1630s, $\delta(H_2O)$; 1478s, 1445m, 1427s, ν(C=C) and ν(C=N); 1259m, 1223s, 1205m, 1160w, 1120w, 1105w, 1051vw, 1036w, δ(C-H) and ν(N-O); 848s, 832s, bending N-O; 776s, 720w, γ(C-H) and aromatic ring deformations; 585m, 538w, 521w, M-O and M-N coordination. From the above peaks the presence of coordinated 2,2'-bpdo is confirmed.[S4]

ICP/MS metals and standard CHN elemental analysis. Anal. Calcd. for $Co_{18}W_{12}C_{226}H_{248}N_{122}O_{98}$ (**1**$^{\mathbf{hyd}}$, M_W = 9508.0 $g\cdot mol^{-1}$): Co, 11.2%; W, 23.2%; C, 28.5%; H, 2.6%; N, 18.0%. Found: Co, 11.4%; W, 22.9%; C, 28.9%; H, 2.4%; N, 18.4%. TGA (Figure S2): loss of 36 H_2O per $\{Co_9W_6\}$ unit, calcd. 13.7 %, found 14.0 %.

Crystal structure determination

Single crystal diffraction data of **1** were collected on a Rigaku R-AXIS RAPID imaging plate area detector with graphite monochromated Mo Kα radiation. Because of easy loss of crystallization solvent molecules in the contact with air, the selected single crystal of **1** was taken directly from the mother solution, dispersed with Apiezon N

grease, and measured at low temperature of T = 80 K. The crystal structure was solved by a direct method using SHELXS-97, and refined by a full-matrix least-squares technique using SHELXL-2014/7.[S5] All further calculations were performed using a WinGX (ver. 1.80.05) integrated system.[S6]

Except of some disordered solvent molecules, all of the non-hydrogen atoms were refined anisotropically. Due to a significant structural disorder, the positions of hydrogen atoms could not be found independently, so the calculations of the ideal positions, and a riding model of the refinement were applied. Due to the symmetry and the untypical coordination of seven 2,2'-bpdo ligands, one of the cluster in the unit cell contains a significant structural disorder related to the coordination sphere of Co5 center for which the 2,2'-bpdo ligand with 50% occupancy coexists with the alternative 50%-occupied coordination of three methanol molecules with the attached hydrogen bonded solvent molecules. This disorder was carefully described by the independently found C, N and O atoms with partial occupancies but their anisotropic refinement needed the application of some restraints on the bond lengths, angles (DFIX), and thermal ellipsoids (DELU, ISOR). Some analogous restrains were also applied for structurally disordered solvent molecules found in the intercluster space. All the restraints were necessary in order to maintain the proper geometries of the 2,2'-bpdo and methanol molecules, and to ensure the convergence of the refinement process. Structural diagrams were prepared using Mercury 3.5.1 software.[S7] CCDC reference number for the crystal structure of **1** is 1416262.

Physical techniques

Magnetic measurements were performed using a Quantum Design 5T SQUID magnetometer. The magnetic data were collected for the grinded single crystals inserted in the glass tube with the small amount of a mother solution. Thus, the obtained data were corrected for the diamagnetic contributions of the compound and the solution using Pascal constants.[S8] The diamagnetic contribution from the glass tube was also taken into account.

Powder X-ray diffraction pattern of polycrystalline sample of **1** sealed in a glass capillary with 0.5 mm of diameter was collected on a PANalytical X'Pert PRO MPD diffractometer with Debye-Scherrer geometry using CuKα radiation (λ =1.54187 Å). The measurement was performed at room temperature.

Infrared spectrum was measured using JASCO FTIR-4100 spectrometer in the 4000 – 500 cm^{-1} range on freshly dried crystals mixed and pressed with KBr. Thermogravimetric measurement was conducted on RIGAKU Thermo Plus TG8120 in the 30 – 400 °C range at a heating rate of 1 $°C \cdot min^{-1}$. The UV-Vis diffuse reflectance spectra were measured by a JASCO V-670 spectrophotometer on freshly dried crystals grinded with $BaSO_4$.

Calculations

Continuous Shape Measure Analysis for coordination spheres of $[W^{V}(CN)_8]^{3-}$ was performed using SHAPE software ver. 2.1.[S9-S10]

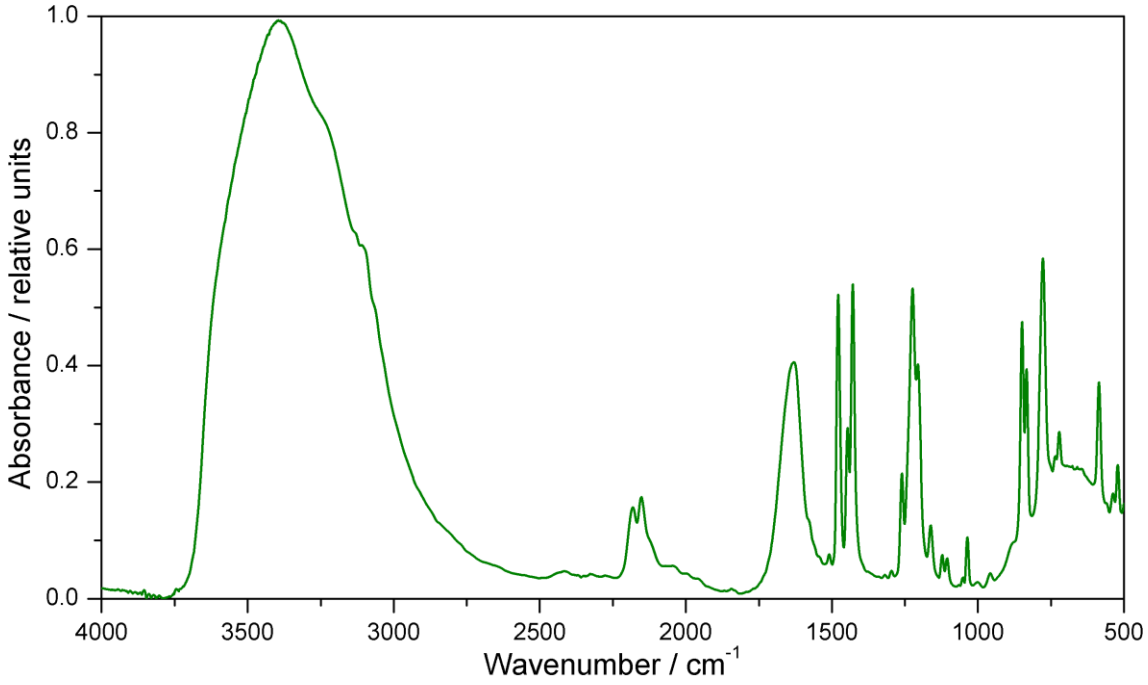

Figure S1. Infrared spectrum of **1** in the 4000 – 500 cm^{-1} range

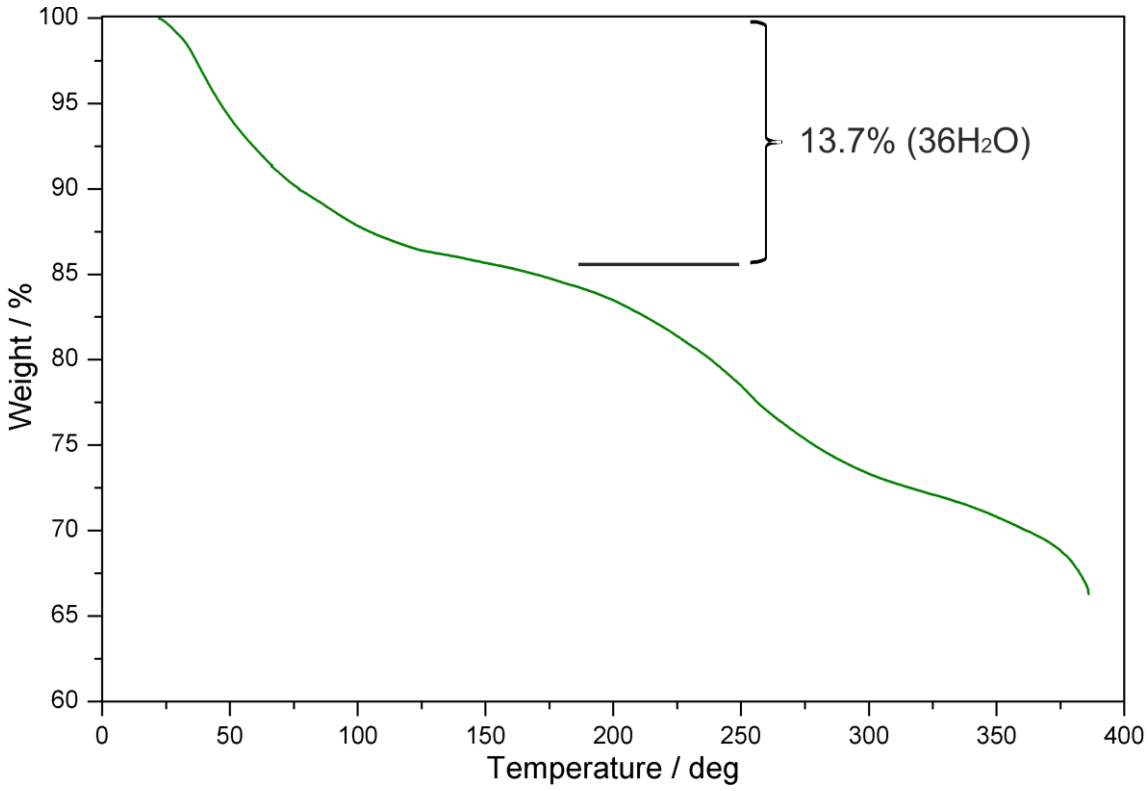

Figure S2. Thermogravimetric curve of **1** with the step related to the loss of crystallization water molecules as typically observed for this compounds' family[S3,S15,S17]

Table S1. Crystal data and structure refinement for **1**

compound		**1**
method		single-crystal XRD
formula		$Co_{18}W_{12}C_{279}H_{156}N_{124}O_{83}$
formula weight [g·mol^{-1}]		9840.1
T [K]		80(2)
λ [Å]		0.71075 (Mo Kα)
crystal system		triclinic
space group		P -1
unit cell	$\boldsymbol{a}$ [Å]	19.1433(3)
	$\boldsymbol{b}$ [Å]	20.6439(4)
	$\boldsymbol{c}$ [Å]	27.4002(5)
	$\boldsymbol{\alpha}$ [deg]	77.864(5)
	$\boldsymbol{\beta}$ [deg]	80.791(6)
	$\boldsymbol{\gamma}$ [deg]	66.500(5)
V [Å^3]		9673.2(5)
Z		1
calculated density [g·cm^{-3}]		1.689
absorption coefficient [cm^{-1}]		4.381
F(000)		4736
crystal size [mm × mm × mm]		0.20 × 0.12 × 0.10
Θ range [deg]		3.001 – 25.242
limiting indices		-24 < h < 24 -26 < k < 26 -35 < l < 34
collected reflections		87018
unique reflections		42555
R_{int}		0.0428
completeness [%]		97.4
max. and min. transmission		0.668 and 0.474
refinement method		full-matrix least-squares on F^2
data/restraints/parameters		42555/126/2354
GOF on F^2		1.267
final R indices		R_1 = 0.0953 [$I > 2\sigma(I)$] wR_2 = 0.1852 (all data)
largest diff peak and hole		3.935 and -2.486 e·A^{-3}

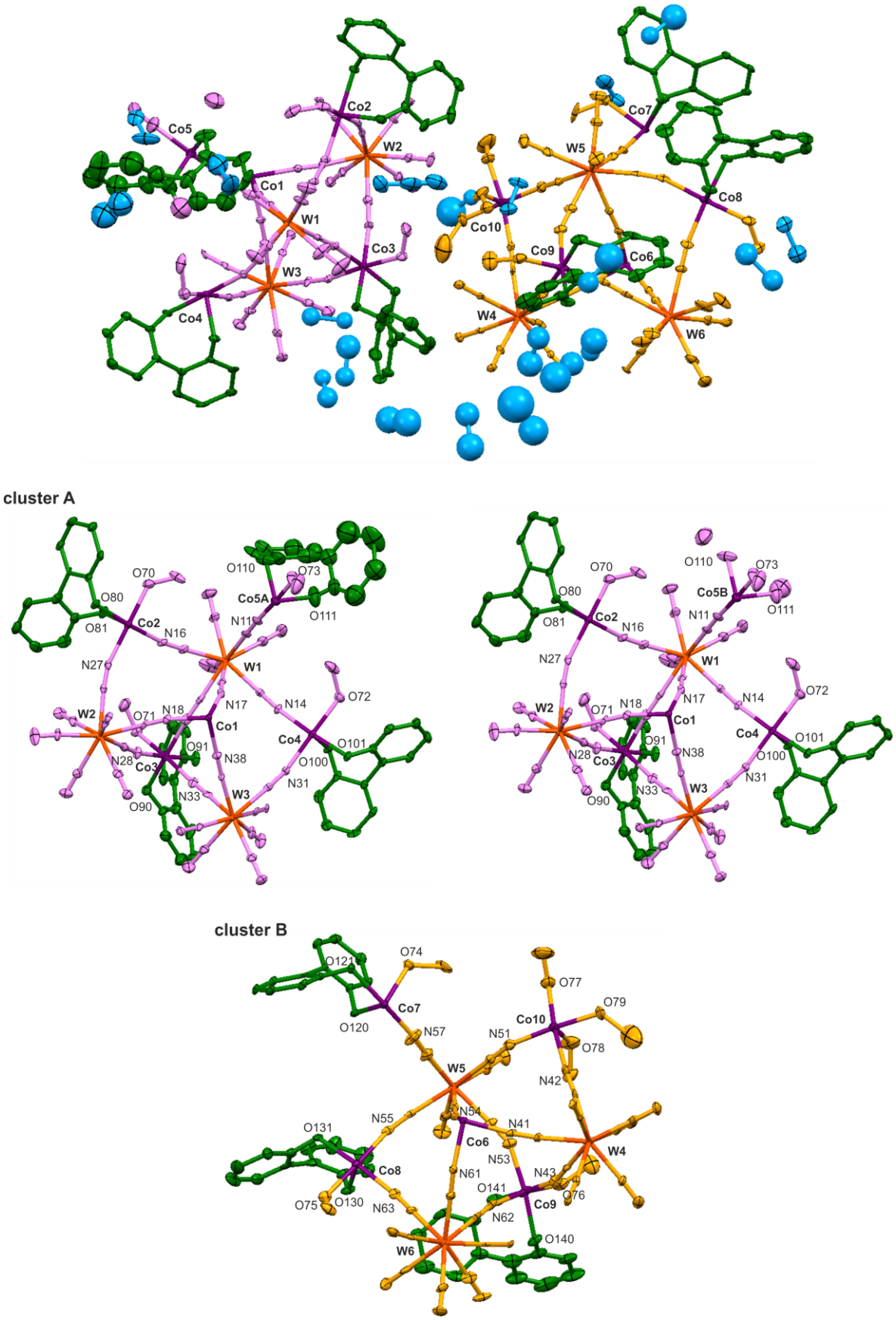

Figure S3. Asymmetric unit of **1** (top) with the detailed insight into the asymmetric parts of cluster A realized with two different Co5 coordination spheres (middle), and of cluster B (bottom).

Table S2. Detailed structure parameters of **1**

Cluster A		**Cluster B**	
Parameter	Value [Å, °]	Parameter	Value [Å, °]
W1 – C	2.121(17) to 2.186(13)	W4 – C	2.131(14) to 2.180(13)
W2 – C	2.144(13) to 2.180(14)	W5 – C	2.137(15) to 2.170(14)
W3 – C	2.132(14) to 2.206(13)	W6 – C	2.114(17) to 2.190(14)
C – N (W1)	1.130(18) to 1.19(2)	C – N (W4)	1.137(17) to 1.171(17)
C – N (W2)	1.120(16) to 1.157(16)	C – N (W5)	1.125(16) to 1.187(18)
C – N (W3)	1.125(18) to 1.164(18)	C – N (W6)	1.127(17) to 1.21(2)
W1 – C - N	174.3(11) to 178.3(14)	W4 – C - N	174.5(11) to 177.3(12)
W2 – C - N	173.8(11) to 179.4(13)	W5 – C - N	174.2(11) to 179.5(14)
W3 – C - N	175.0(11) to 179.1(16)	W6 – C - N	174.4(12) to 179(3)
Co1 – N (CN)	2.076(11) 2.098(10) 2.100(11)	Co6 – N (CN)	2.071(11) 2.088(10) 2.113(11)
Co2 – N(CN)	2.088(11) 2.105(11) 2.125(11)	Co7 – N(CN)	2.077(10) 2.104(10) 2.106(11)
Co2 – O(MeOH)	2.122(11)	Co7 – O(MeOH)	2.169(9)
Co2 – O(2,2'-bpdo)	2.070(10) 2.093(9)	Co7 – O(2,2'-bpdo)	2.066(9) 2.089(9)
Co3 – N(CN)	2.071(13) 2.073(12) 2.087(11)	Co8 – N(CN)	2.059(11) 2.123(13) 2.124(11)
Co3 – O(MeOH)	2.133(9)	Co8 – O(MeOH)	2.125(12)
Co3 – O(2,2'-bpdo)	2.036(10) 2.082(10)	Co8 – O(2,2'-bpdo)	2.075(9) 2.092(9)
Co4 – N(CN)	2.073(10) 2.119(10) 2.123(11)	Co9 – N(CN)	2.045(12) 2.091(13) 2.099(12)
Co4 – O(MeOH)	2.160(10)	Co9 – O(MeOH)	2.098(11)
Co4 – O(2,2'-bpdo)	2.066(9) 2.082(9)	Co9 – O(2,2'-bpdo)	2.044(11) 2.072(10)
Co5 – N(CN)	2.057(14) 2.074(13) 2.094(11)	Co10 – N(CN)	2.051(12) 2.079(15) 2.095(13)
Co5 – O(MeOH)	2.103(14) 2.079(14) 2.092(15)	Co10 – O(MeOH)	2.087(11) 2.089(14) 2.114(11)
Co5 – O(2,2'-bpdo)	2.079(14) 2.092(15)	Co10 – O(2,2'-bpdo)	no 2,2'-bpdo

Cluster A		Cluster B	
Parameter	Value [Å, °]	Parameter	Value [Å, °]
Co1 – N – C (CN)	164.7(10) 168.3(11) 176.5(11)	Co6 – N – C (CN)	162.7(11) 163.4(10) 173.8(10)
Co2 – N – C (CN)	163.8(10) 169.0(10) 169.5(11)	Co7 – N – C (CN)	164.8(10) 167.0(11) 168.1(10)
Co3 – N – C (CN)	168.3(10) 170.2(11) 172.6(11)	Co8 – N – C (CN)	160.9(10) 169.1(10) 168.9(13)
Co4 – N – C (CN)	163.6(10) 166.2(10) 168.8(10)	Co9 – N – C (CN)	155.1(13) 160.4(11) 167.7(11)
Co5 – N – C (CN)	170.0(12) 171.8(11) 174.9(12)	Co10 – N – C (CN)	162.2(11) 163.1(11) 173.5(11)
N – Co1 – N	180, 180, 180 86.4(4), 88.1(4), 88.4(4)	N – Co6 – N	180, 180, 180 86.3(4), 87.8(4), 89.6(4)
N – Co2 – O	165.5(4) 176.5(4) 179.3(4)	N – Co7 – O	162.9(4) 175.2(4) 175.9(4)
O – Co2 – O(2,2’-bpdo)	83.2(4)	O – Co7 – O (2,2’-bpdo)	82.3(4)
py – py torsion (2,2’bpdo for Co2)	51.6	py – py torsion (2,2’bpdo for Co7)	52.0
N – Co3 – O	169.0(4) 175.7(4) 176.9(4)	N – Co8 – O	166.3(4) 175.8(4) 178.2(4)
O – Co3 – O(2,2’-bpdo)	83.5(4)	O – Co8 – O (2,2’-bpdo)	82.4(4)
py – py torsion (2,2’bpdo for Co3)	51.8	py – py torsion (2,2’bpdo for Co8)	49.9
N – Co4 – O	162.9(4) 176.4(4) 176.5(4)	N – Co9 – O	172.2(4) 172.5(5) 176.8(5)
O – Co4 – O(2,2’-bpdo)	83.0(3)	O – Co9 – O (2,2’-bpdo)	86.0(4)
py – py torsion (2,2’bpdo for Co4)	53.6	py – py torsion (2,2’bpdo for Co9)	54.0
N – Co5 – O	174.4(6) 177.5(6) 177.7(6)	N – Co10 – O	172.7(5) 173.8(5) 175.3(5)
O – Co5 –O (2,2’-bpdo)	85.4(7)	O – Co10 –O(2,2’-bpdo)	no 2,2’-bpdo
py – py torsion (2,2’bpdo for Co5)	63.0	py – py torsion (2,2’bpdo for Co10)	no 2,2’-bpdo

Table S3. Results of Continuous Shape Measure Analysis for $[W^{V}(CN)_8]^{3-}$ units in **1**

W centre	CSM parameters*			Geometry
	BTP – 8	SAPR – 8	DD – 8	
Cluster A				
W1	1.810	2.504	**0.320**	DD-8
W2	1.809	1.868	**0.384**	DD-8
W3	1.148	1.238	**0.777**	DD-8 admixture of BTP-8
Cluster B				
W4	1.186	1.631	**0.613**	DD-8 admixture of BTP-8
W5	1.487	**0.711**	1.139	SAPR-8 admixture of DD-8
W6	**1.049**	**0.934**	1.636	intermediate SAPR-8/BTP-8

* CSM parameters:[S9-S10]
CSM BTP-8 – the parameter related to the bicapped trigonal prism geometry (C_{2v} symmetry)
CSM SAPR-8 – the parameter related to the square antiprism (D_{4d} symmetry)
CSM DD-8 – the parameter related to the dodecahedron (D_{2d} symmetry)
CSM = 0 for the ideal geometry and increase with the increasing distortion for the ideal polyhedron.

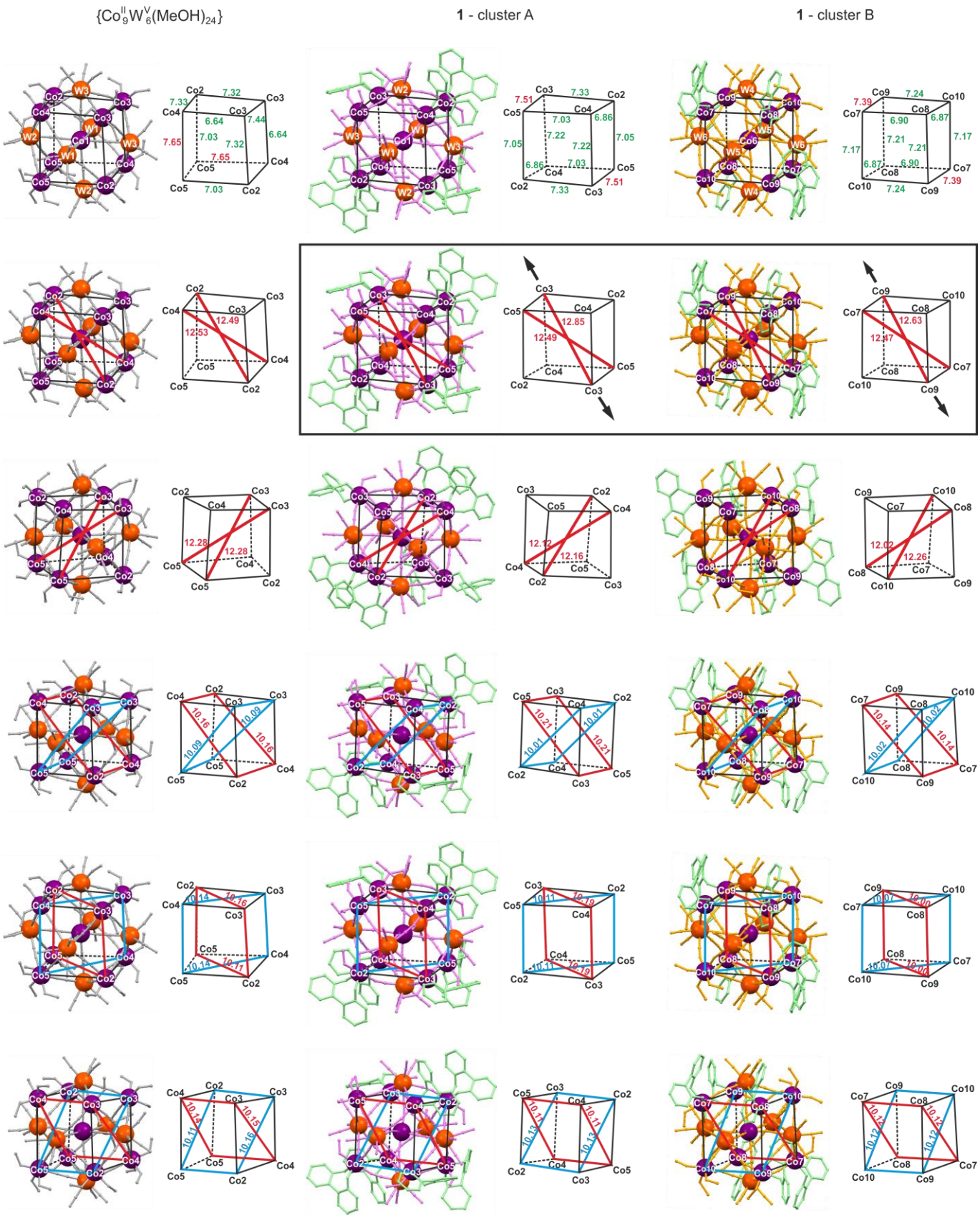

Figure S4. Deformations of the {Co$^{II}_8$} pseudo-cubic moieties of the cluster cores of **1** (clusters A and B) in respect to the purely solvated {Co$^{II}_9$W$^{V}_6$(MeOH)$_{24}$} molecule.[S11] All metric parameters are depicted in [Å] units. The arrows correspond to the directions of the strongest elongation of the analyzed {Co$^{II}_8$} polyhedrons.

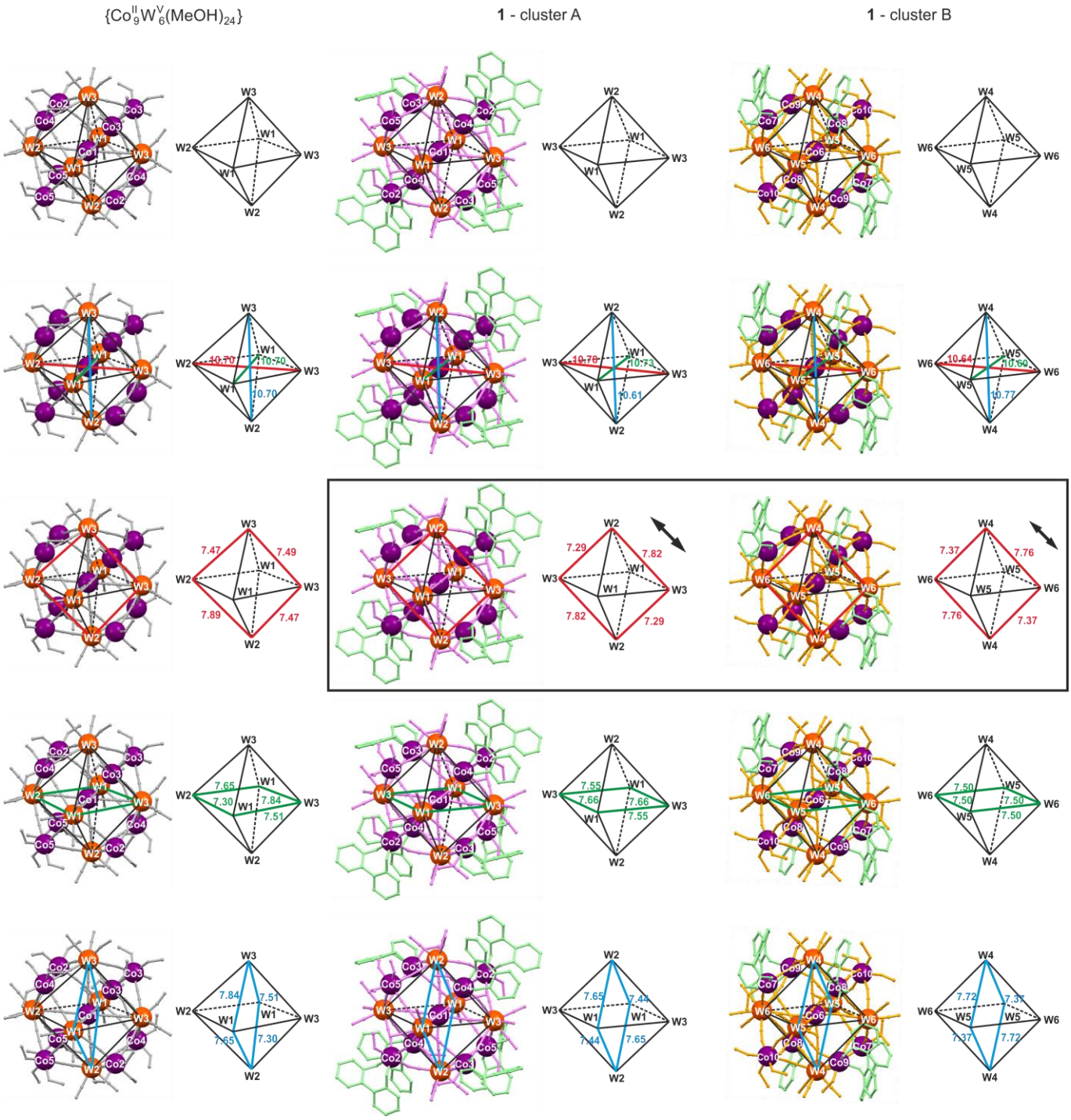

Figure S5. Deformations of the {W^{V}_6} pseudo-octahedral moieties of the cluster cores of **1** (clusters A and B) in respect to the purely solvated {$Co^{II}_9W^{V}_6(MeOH)_{24}$} molecule.[S11] All metric parameters are depicted in [Å] units. The arrows correspond to the directions of the strongest elongation of the analyzed {W^{V}_6} polyhedrons.

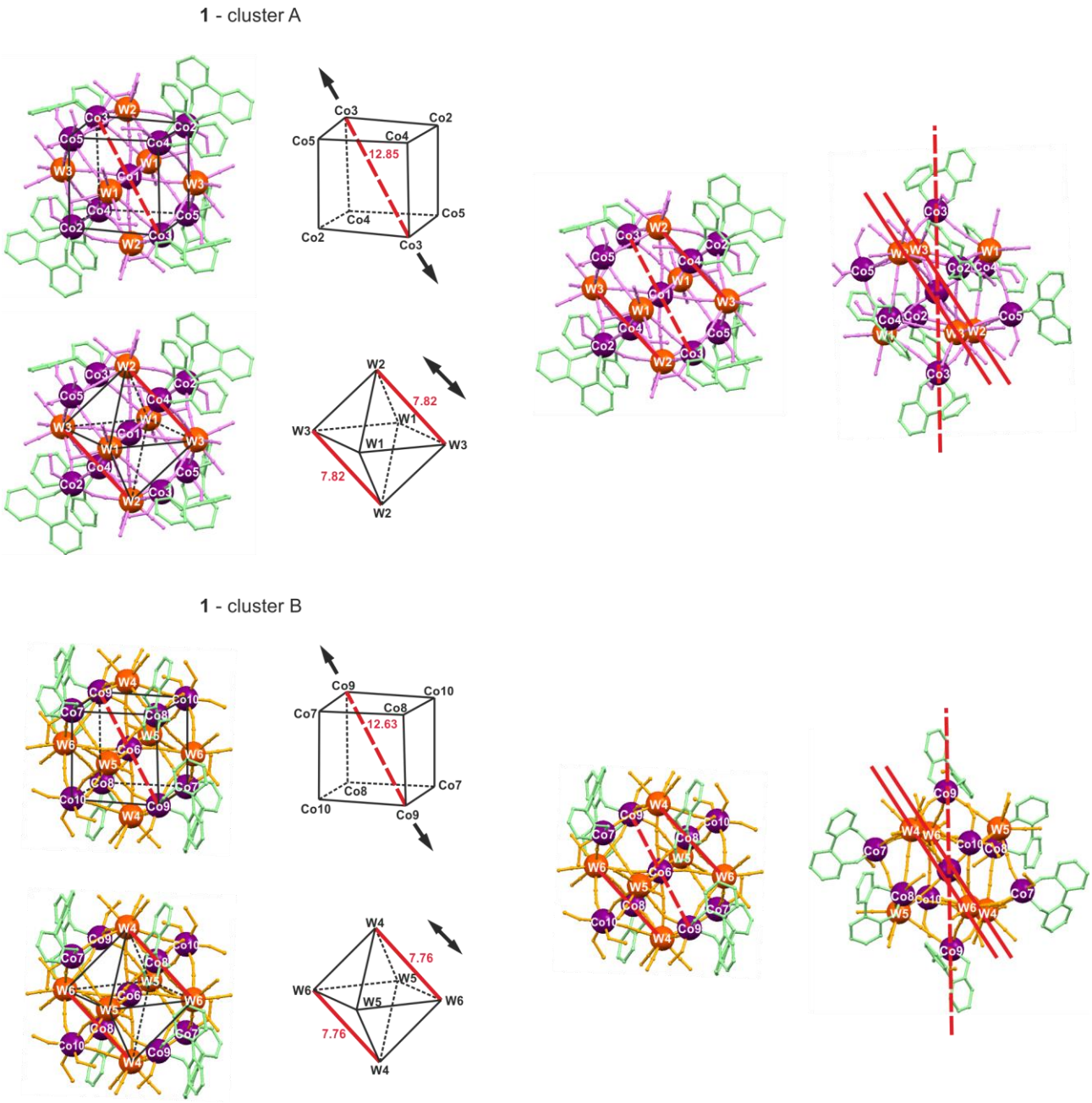

Figure S6. Comparison of the directional deformations of the $\{Co^{II}_8\}$ pseudo-cubic, and the $\{W^{V}_6\}$ pseudo-octahedral fragments of the cluster cores of **1** (clusters A and B). All metric parameters are depicted in [Å] units. The red lines and arrows correspond to the directions of the strongest elongation of the polyhedrons. The approximate angle between the elongation directions for $\{Co^{II}_8\}$ and $\{W^{V}_6\}$ units is ca. 40 degree for both types of clusters.

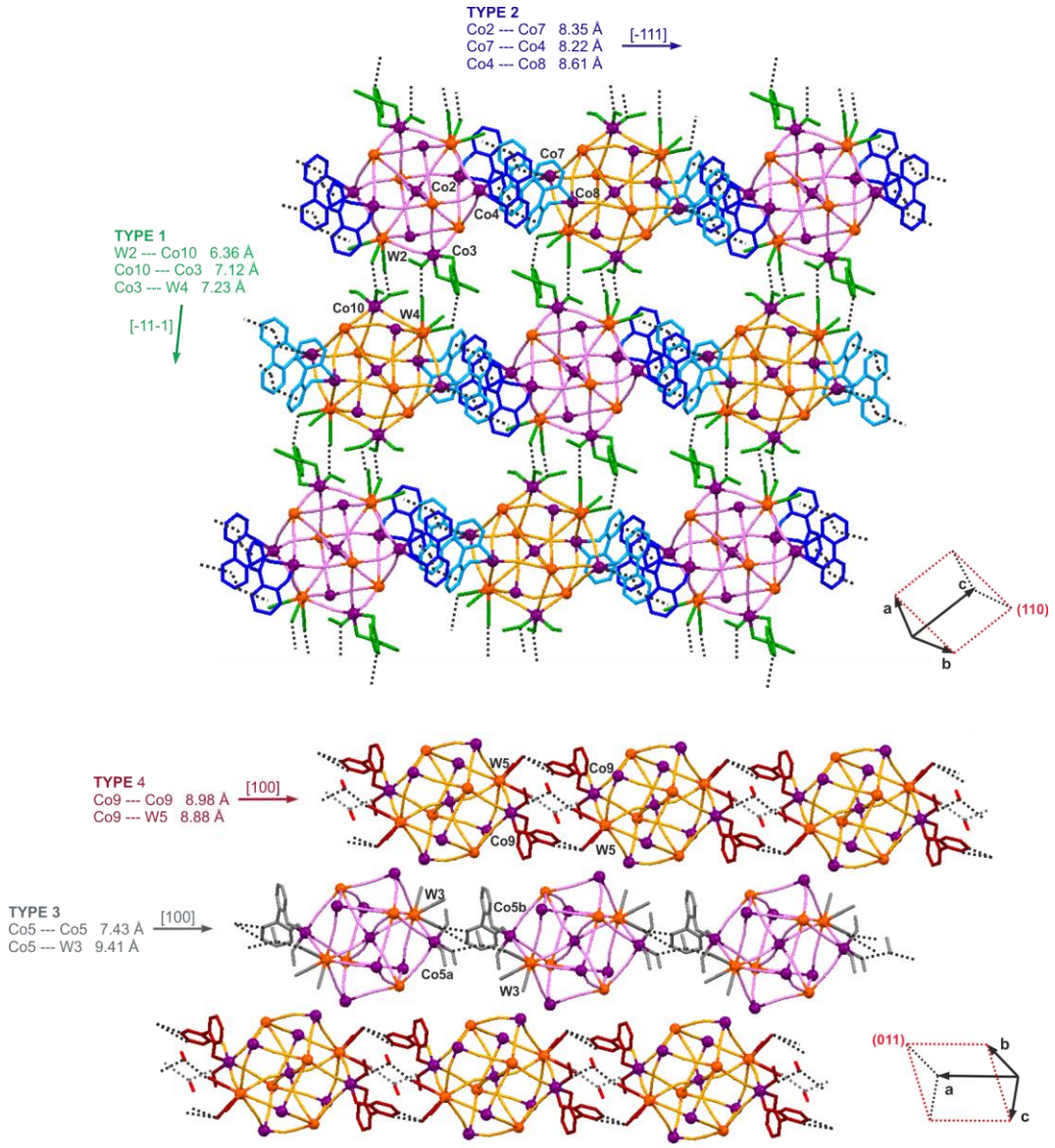

Figure S7. The supramolecular arrangement of $\{Co^{II}_{9}W^{V}_{6}\}$ molecules in **1** with the insight into four main types of intercluster interactions, and the closest metal-metal intermolecular distances. The cyanido-bridged core of the cluster A is presented by light purple, and that of the cluster B by the light orange sticks. Dotted lines correspond to hydrogen bonds and π-π interactions.

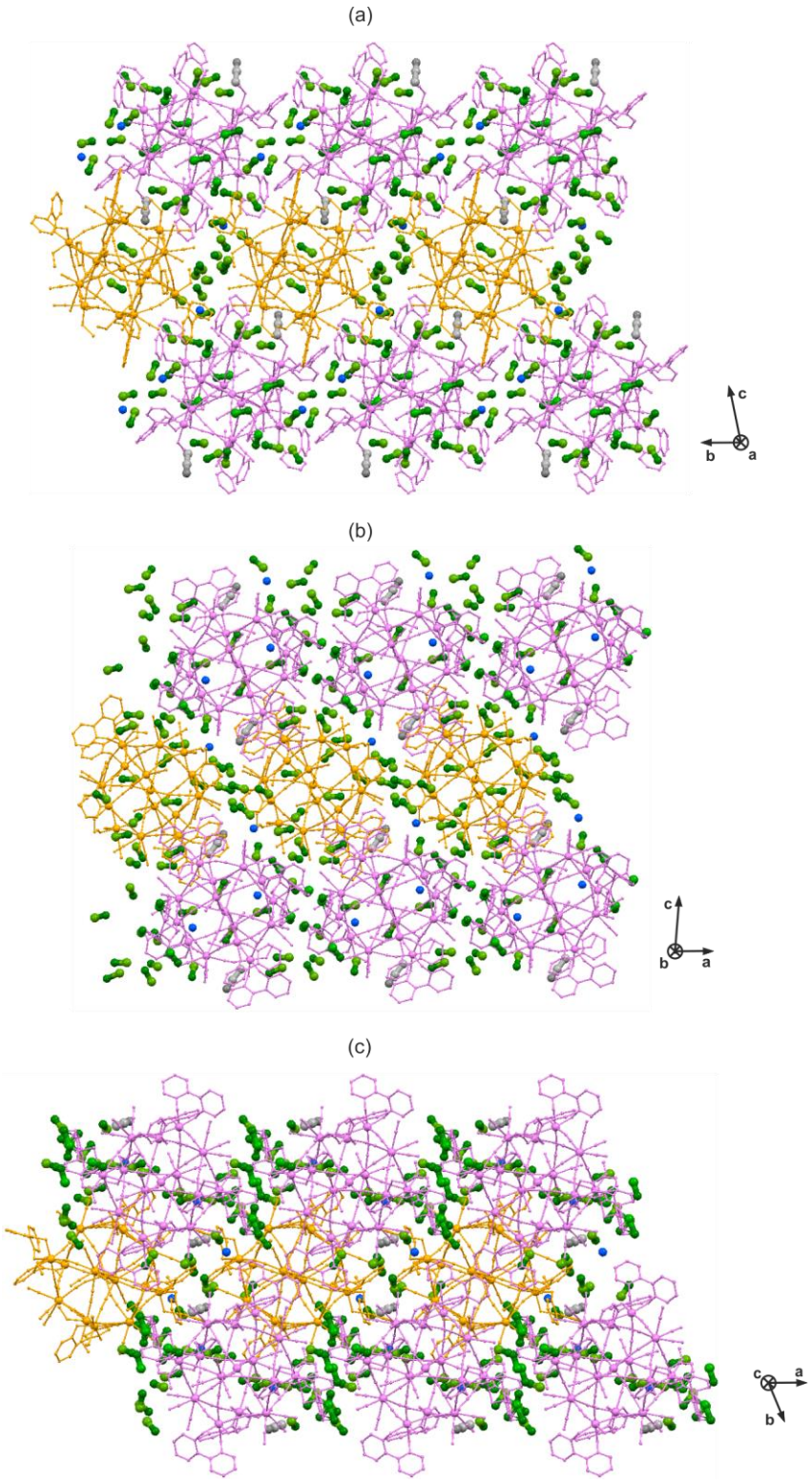

Figure S8. The supramolecular arrangement of cyanido-bridged clusters and crystallization solvent molecules of water (blue), methanol (green), and acetonitrile (grey) in the crystal structure of **1** presented in the views along **a**, **b**, and **c** crystallographic directions (a, b, and c, respectively). The two types of cyanido-bridged clusters were distinguished by colors: light violet for cluster A, orange for cluster B. Hydrogen atoms are omitted for clarity.

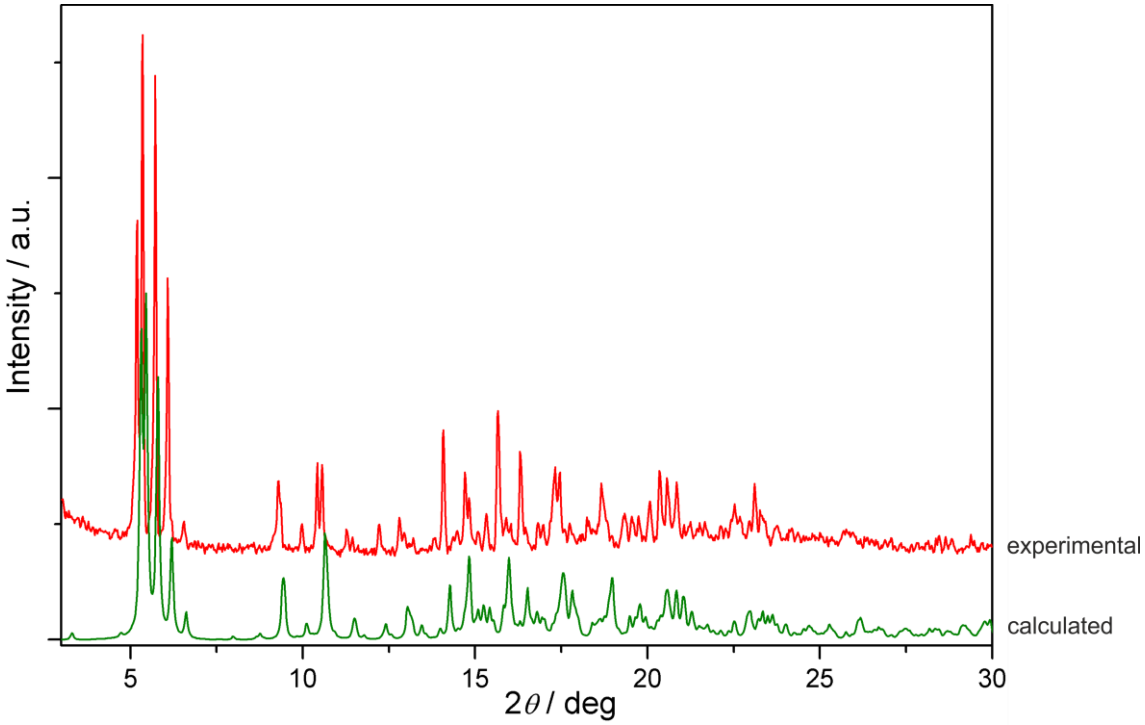

Figure S9. Experimental and calculated (from the single crystal X-ray model) powder X-ray diffraction patterns of **1** in the representative 3–30° range of 2Θ angle. The consequent shift of all peaks between the experimental and the calculated patterns is due to the standard temperature effect, as the PXRD experiment was performed at room temperature, while the single-crystal X-ray measurement was done at low temperature of 80 K.

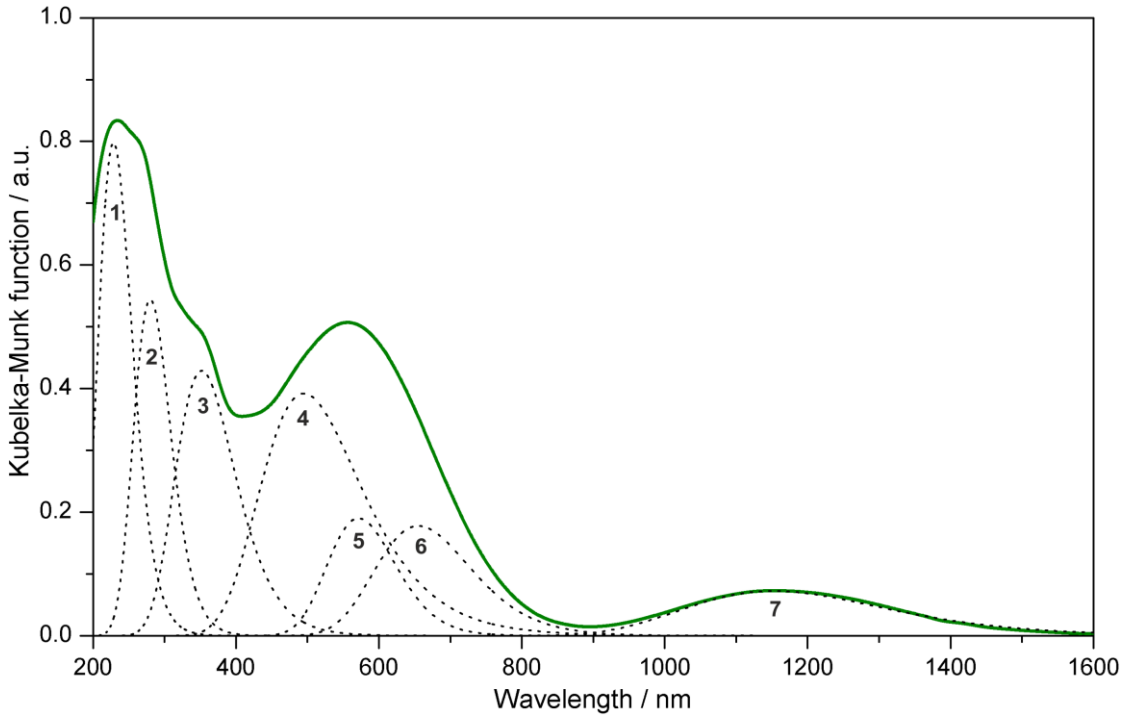

Figure S10. UV-Vis-NIR diffuse reflectance spectrum of **1** in the 200 – 1600 nm range. Green line represents the experimental spectrum while the dotted lines show the results of the deconvolution of the spectrum into seven peaks interpreted in Table S4.

Table S4. Analysis of UV-Vis-NIR diffuse reflectance spectrum of **1**

Peak	Position of maximum / nm	Interpretation
1	230	combined contributions from π-π* transitions of 2,2'-bpdo ligands and metal-to-ligand charge transfer (MLCT) and ligand-to-metal charge transfer (LMCT) transitions within $[W^{V}(CN)_8]^{3-}$ ions[S12]
2	280	
3	355	ligand-to-metal charge transfer (LMCT) transitions within $[W^{V}(CN)_8]^{3-}$ ions
4	495	$Co^{II} – W^{V} \rightarrow Co^{III} – W^{IV}$ metal-to-metal charge transfer (MMCT) transition[S13-S15]
5	570	d-d (ligand field, LF) transition of Co^{II}, $^4T_{1g}(^4F) \rightarrow {}^4T_{1g}(^4P)$[S16]
6	650	d-d (LF) transition of Co^{II}, $^4T_{1g}(^4F) \rightarrow {}^4A_{2g}(^4F)$
7	1150	d-d (LF) transition of Co^{II}, $^4T_{1g}(^4F) \rightarrow {}^4T_{2g}(^4F)$

Detailed discussion on the *dc* magnetic properties of 1

Temperature dependence of molar magnetic susceptibility, $\chi_M T(T)$ at H_{dc} = 1000 Oe, and the field dependence of magnetization, $M(H)$ at T = 1.8 K, of **1** are presented in Figure 2. Room temperature $\chi_M T$ value for two $\{Co_9W_6\}$ units is 58.5 $cm^3mol^{-1}K$ corresponding well to the 54–66 $cm^3mol^{-1}K$ range calculated for the isolated eighteen Co^{II} and twelve W^V when applying the standard parameters for $[W^V(CN)_8]^{3-}$ ions (S_W = 1/2, g_W = 2.0), and the spin of 3/2 with the typical 2.4–2.7 range for *g*–factor which is characteristic of six coordinated Co^{II} complexes with distorted octahedral geometry when magnetic properties at high temperatures are considered.[S11-S14]

On cooling, the $\chi_M T$ grows slowly and continuously to the maximum value of 88.2 $cm^3mol^{-1}K$ at 5 K. This suggests predominant ferromagnetic coupling as for the antiferromagnetic interactions at least the shallow minimum should be expected, especially in the presence of pseudo-octahedral Co^{II} centers exhibiting the intrinsic decrease of $\chi_M T$ upon cooling due to the spin-orbit coupling effect.[S21] Further decrease of $\chi_M T$ below 5 K to the lowest temperatures is observed, and it can be reasonably explained partially by zero-field splitting on Co^{II}, and, more importantly, by the occurrence of antiferromagnetic intercluster interactions which can easily operate at very low temperatures in **1** due to relatively short intercluster distance of 6.36 Å between W2 and Co10 centers, along [-11-1] axis.[S15,S20]

The better determination of the type of cyanide-mediated Co–W magnetic interactions in **1**, and the resulting magnetic ground state of $\{Co^{II}{}_9W^V{}_6\}$ clusters, is usually possible through the analysis of two experimental parameters: (*a*) the value of $\chi_M T$ at the low temperature maximum, and (*b*) the value of saturation magnetization at the low temperature of 1.8 K which can be estimated by the value of magnetization at the high field of 50 kOe, even if the saturation of magnetization is usually not complete at this field due to the large magnetic anisotropy. The comparison of these two parameters with the theoretically predicted values gives commonly the reasonable conclusion about the intracluster magnetic interactions.[S15,S20,S22-S26] For the case of **1**, the maximum of $\chi_M T$ at 5 K for two $\{Co_9W_6\}$ units is $\chi_M T_{max}$ = 88.2 $cm^3mol^{-1}K$, and the related magnetization for 50 kOe at T = 1.8 K is M_S = 35.1 Nβ.

The theoretical values of $\chi_M T_{max}$ and M_S can be calculated using the standard parameters of W^V: S_W = 1/2, g_W = 2.0, and the broadly applied effective spin approach for pseudo-octahedral high spin Co^{II} centers which magnetism is well approximated by the effective spin of $S_{Co,LT}$ = 1/2, and the average *g*-factor for the powder sample of 4.3–4.4.[S16,S21-S27] Within this approach, the two general cases can be considered:

(a) ferromagnetic (F) ground state: the ground state spin should be 15/2 with the average *g*-factor of 3.38–3.44; it results in the $\chi_M T_{max}$ in the range of 91.0–94.3 $cm^3mol^{-1}K$, and the M_S within the range of 25.4–25.8 Nβ which produce $\chi_M T_{max}$ = 182.0–188.6 $cm^3mol^{-1}K$ and M_S = 50.8–51.6 Nβ for two $\{Co_9W_6\}$ units.

(b) antiferromagnetic (AF) ground state: the ground state spin should be 3/2 with the average *g*-factor of 3.38–3.44; it results in the $\chi_M T_{max}$ in the range of 5.4–5.6 $cm^3mol^{-1}K$, and the M_S within the range of 5.1–5.2 Nβ which produce $\chi_M T_{max}$ = 10.8–11.2 $cm^3mol^{-1}K$ and M_S = 10.2–10.4 Nβ for two $\{Co_9W_6\}$ units.

As compared with the experimental values, neither the pure ferromagnetic nor the antiferromagnetic ground state can be ascribed to the clusters of **1**.

The alternative, sometimes postulated, treatment of octahedral Co^{II} complexes includes the validity of $S = 3/2$ at low temperatures with the *g*-factors in the range of 2.4–2.7.[S28-S29] Within this approach, again the two general cases can be considered:

(a) ferromagnetic ground state: the ground state spin should be 33/2 with the average *g*-factor of 2.24–2.42; it results in the $\chi_M T_{max}$ in the range of 181.0–211.4 $cm^3mol^{-1}K$, and the M_S within the range of 37.0–39.9 Nβ which produce $\chi_M T_{max}$ = 362.0–422.8 $cm^3mol^{-1}K$ and M_S = 74.0–79.8 Nβ for two $\{Co_9W_6\}$ units.

(b) antiferromagnetic ground state: the ground state spin should be 21/2 with the average g-factor of 2.24–2.42; it results in the $\chi_M T_{max}$ in the range of 75.7–88.4 $cm^3mol^{-1}K$, and the M_S within the range of 23.5–25.4 Nβ which produce $\chi_M T_{max}$ = 151.4–176.8 $cm^3mol^{-1}K$ and M_S = 47.0–50.8 Nβ for two $\{Co_9W_6\}$ units.

As compared with the experimental values, neither the ferromagnetic nor the antiferromagnetic ground state can be ascribed to the clusters in **1** as the experimental values are situated well below the expected values for both possibilities.

The above consideration indicates that the pure ferromagnetic or antiferromagnetic ground state of clusters in **1** cannot be postulated. However, the values $\chi_M T_{max}$ and M_S in **1** are between the expected ranges for F and AF states calculated within the effective spin approach, which in fact is usually used in the description of *dc* magnetic properties of $\{Co_9W_6\}$ clusters.[S15,S20,S30] This suggests that the observed magnetism of **1** could be explained by the mixed AF–F interactions giving the intermediate ground state spin.

We checked various possibilities of average intermediate ground spin states of **1** between the AF limit of 3/2 and F limit of 15/2, and we found that ground state spin of 11/2 with the average *g*-factor of 3.38–3.44 can reasonably suit to the experimental data. In such a case, the $\chi_M T_{max}$ should be in the range of 51.0–52.9 $cm^3mol^{-1}K$ which produces $\chi_M T_{max}$ = 102.0-105.8 $cm^3mol^{-1}K$, while the saturation magnetization, M_S within the range of 18.6–18.9 Nβ giving the range of 37.2–37.8 Nβ for two $\{Co_9W_6\}$ clusters. The experimental values of **1**, $\chi_M T_{max}$ = 88.2 $cm^3mol^{-1}K$ and M_S = 35.1 Nβ correspond fairly well to these theoretical limits. It is important to notice that these calculations are rather rough as two different clusters were detected in **1**, and they can differ in the magnetic ground state, giving even more complex scheme of magnetic interactions, which is far beyond our analysis.

As presented above, the mixed AF–F scheme of Co-W interactions can reasonably explain the *dc* magnetic properties. It is also supported by our latest findings on the Co-W magnetic systems as the co-existence of mixed AF-F interactions within one coordination system was presented in Co-W chiral chains,[S17] and discrete $\{Co_3W_2\}$ molecules.[S19] These reports showed that subtle changes in the geometries of Co^{II} centers, even without the differences in the type of ligands' donor atoms, together with the changes in geometries of cyanide bridges, can modify significantly the strength of magnetic coupling, or even give both the antiferromagnetic and ferromagnetic type of Co-W magnetic interaction. Such a situation is presumably observed in **1**, especially in strongly deformed clusters A but the detailed analysis is now not achievable due to many different Co^{II} complexes of probably various single-ion anisotropies, and overall complex topology of the clusters.

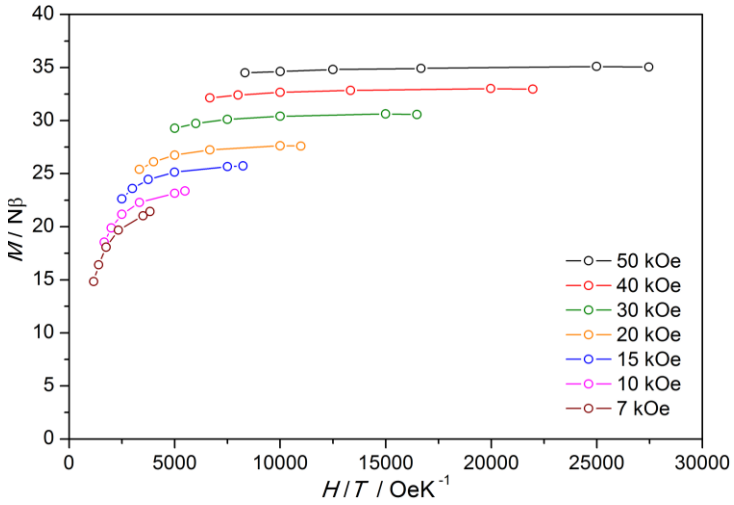

Figure S11. Reduced magnetization versus field curves of **1** in the 1.8–6 K range. The non-superposition of the curves under various fields indicates the presence of significant magnetic anisotropy. The detailed analysis, involving the estimation of *D* parameter, cannot be, however, performed due to the difficulties in the determination of the ground state spin (see above), and the presence of two different clusters in the crystal structure of **1**.

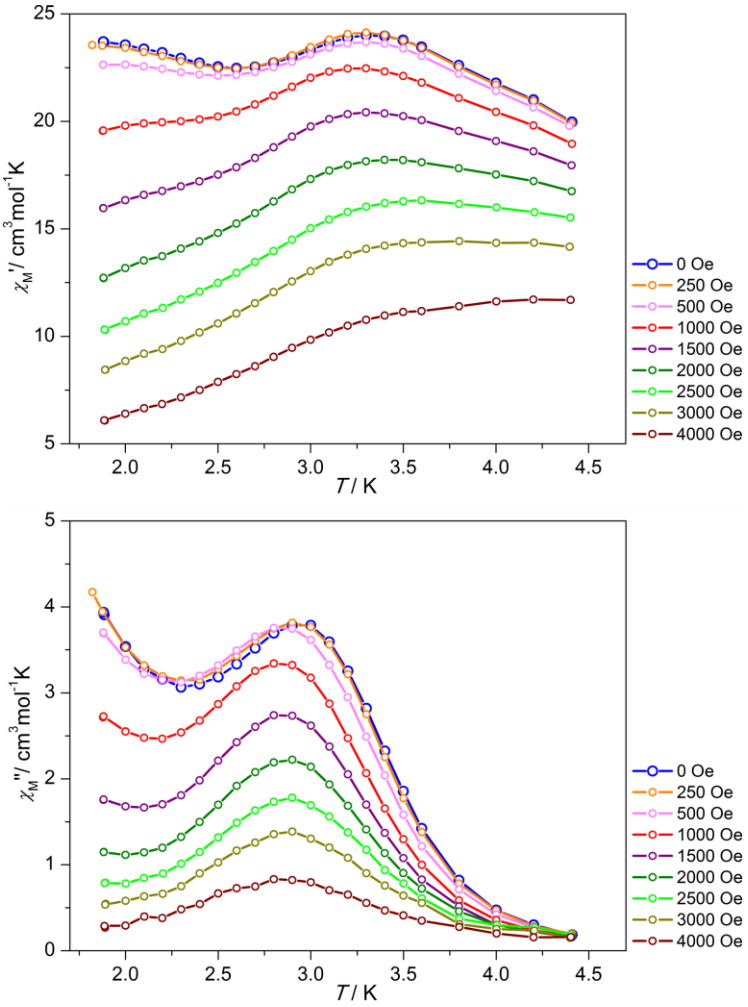

Figure S12. Temperature dependences of in-plane χ_M' and out-of-plane χ_M'' magnetic susceptibility of **1** under *ac* magnetic field of 3 Oe with the frequency of 1500 Hz, and various indicated *dc* magnetic fields.

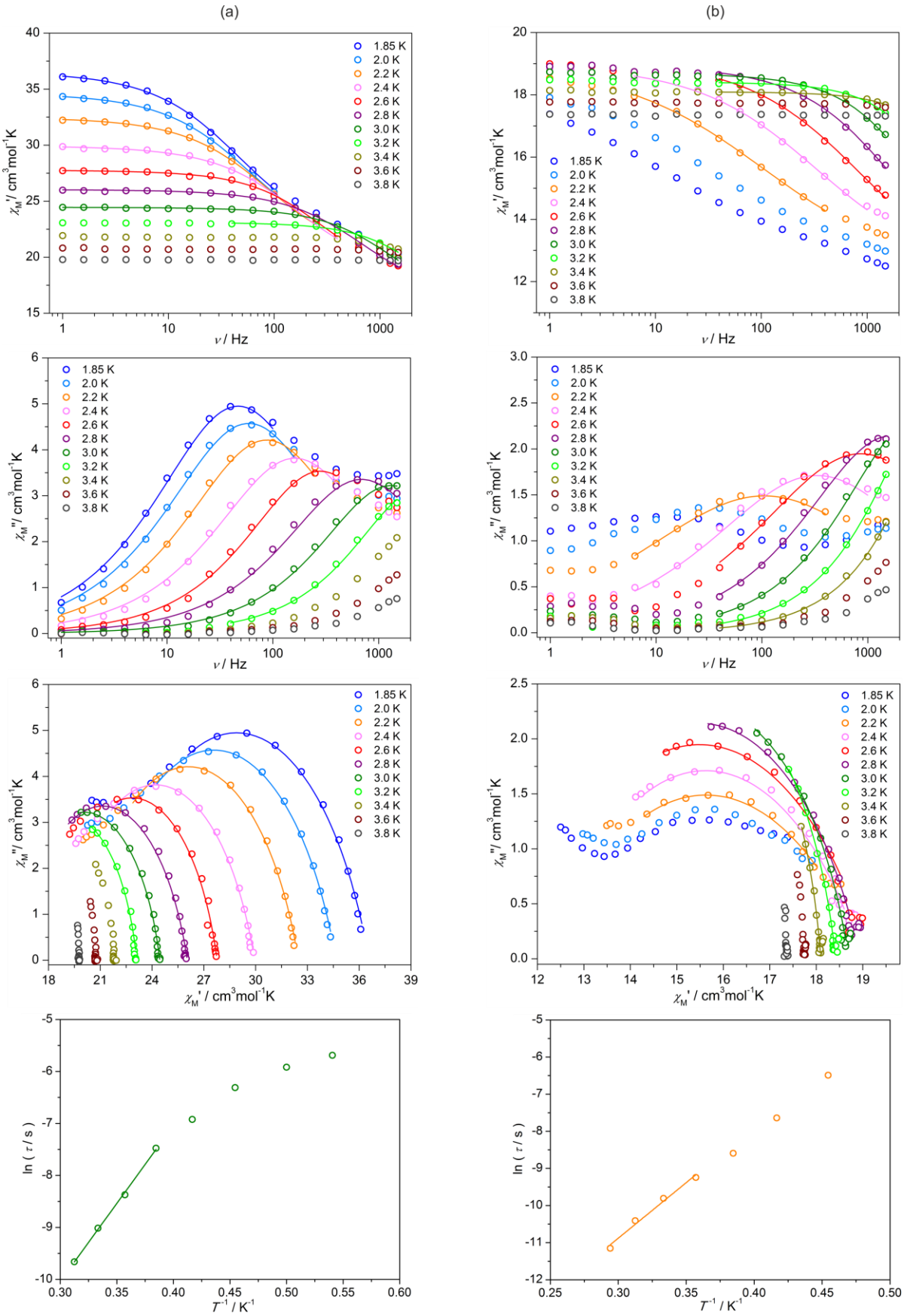

Figure S13. Comparison of *ac* magnetic data of **1** measured at 0 Oe (a) and 2000 Oe (b) *dc* external fields, including the $\chi_M'(\nu)$, $\chi_M''(\nu)$, $\chi_M''(\chi_M')$, and $\ln(\tau)(T^{-1})$ plots. The solid lines to the fitting according to the Cole-Cole model for $\chi_M'(\nu)$, $\chi_M''(\nu)$, and $\chi_M''(\chi_M')$ plots, and the Arrhenius law for the $\ln(\tau)(T^{-1})$ plot.

Table S5. Parameters obtained by fitting the Cole–Cole χ_M"–χ_M' plots of **1** using the generalized Debye model.

magnetic *dc* field (figure no.)	*T* [K]	χ_0 [cm^{3}mol^{-1}]	χ_∞ [cm^{3}mol^{-1}]	τ [ms]	α
0 Oe (figure S12a)	1.85	36.57(8)	21.2(3)	3.38(13)	0.270(12)
	2.0	34.66(6)	20.5(2)	2.69(8)	0.269(10)
	2.2	32.48(5)	19.72(19)	1.82(6)	0.257(10)
	2.4	29.94(5)	18.5(2)	0.98(4)	0.253(12)
	2.6	27.76(3)	17.9(2)	0.57(3)	0.206(13)
	2.8	26.04(3)	16.24(17)	0.232(8)	0.235(11)
	3.0	24.45(2)	15.7(2)	0.126(5)	0.192(11)
	3.2	23.10(3)	15.1(4)	0.064(6)	0.155(19)
2000 Oe (figure S12b)	2.2	19.04(7)	12.21(13)	1.52(7)	0.477(14)
	2.4	18.98(7)	12.3(2)	0.48(4)	0.401(19)
	2.6	19.18(6)	11.80(18)	0.186(11)	0.382(16)
	2.8	18.94(4)	12.1(2)	0.097(6)	0.292(15)
	3.0	18.697(19)	12.2(3)	0.055(4)	0.209(14)
	3.2	18.415(9)	11.8(4)	0.030(3)	0.145(12)
	3.4	18.098(10)	10.2(16)	0.014(4)	0.11(2)

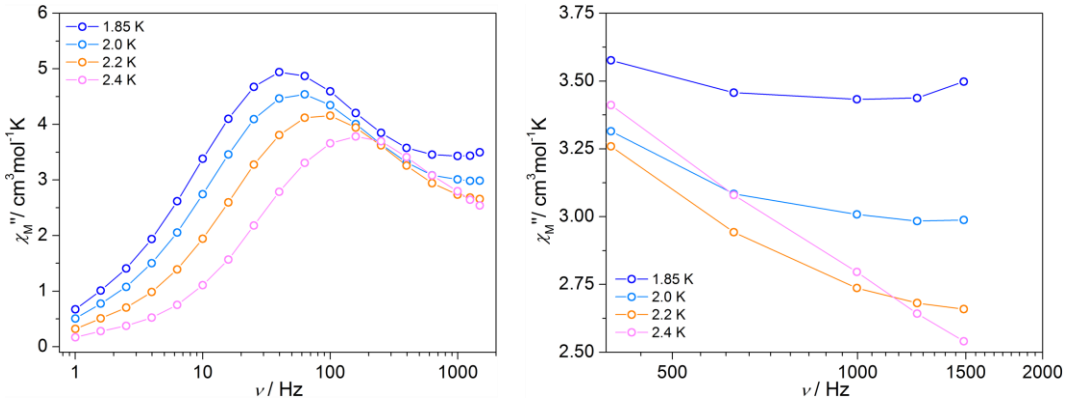

Figure S14. The detailed insight into χ_M"(ν) plot of **1** at zero *dc* field at the lowest temperatures of 1.85, 2.0, 2.2, and 2.4 K with the magnification of the highest frequencies range showing the onset of the second relaxation process occurring for highest frequencies at the lowest temperatures. The solid lines are here only to guide the eye.

Detailed discussion on the structural anisotropy influencing the SMM behaviour of clusters A and B of 1

As presented in the magnetic results (Figures 3 and S13), they are two distinguishable relaxation processes occurring in **1**. The first relaxation process is starting to appear below 5 K which is the significant enhancement when compared with the original, purely solvated $\{Co_9(MeOH)_{24}W_6\}$ clusters, their reported derivatives, and the other $\{M_9W_6\}$ molecules. The second relaxation process appears as a tail in the temperature dependence of χ_M" below 2.5 K which is similar to the other reported $\{Co_9W_6\}$ molecules capped by eight bidentate ligands, or combined into one dimensional coordination polymer by organic bridges (Figure S15).

The presence of two relaxation processes in **1** can be reasonably explained by the two structurally distinct $\{Co_9W_6\}$ clusters (A and B, Figures 1 and S4–S8) detected in the crystal structure of **1**. It is, however, a challenging task to assign these two different relaxation processes to the specific clusters as the origin of the magnetic anisotropy in these type of cyanido-bridged molecules is quite complex.[S31-S33] In general, it was reported that the magnetic anisotropy of Co^{II}-$[W^{V}(CN)_8]^{3-}$ coordination systems depends mainly on the single-ion anisotropies of individual Co^{II} complexes while nearly isotropic $[W^{V}(CN)_8]^{3-}$ ions ensures only the presence of magnetic interactions giving small or even negligible contribution to the magnetic anisotropy.[S19-S20] Thus, the clusters A and B of **1** should be discussed from the viewpoint of magnetic anisotropies of the embedded Co^{II} centers, and their relative positions within the cluster core. This can be achieved precisely with the support of the theoretical *ab initio* calculations of single-ion anisotropies, involving the type of anisotropy and the eventual direction of the easy magnetic axis, of Co^{II} centers as the relationship between the structural features of pseudo-octahedral Co^{II} and its magnetic anisotropy can be complicated.[S19-S20] However, the presence of large magnetic anisotropy of Co^{II} can be often correlated with the significant elongation of the distorted octahedral geometry.[S17]

Therefore, we decided to inspect the related elongations of the Co^{II} complexes of clusters A (Co1–Co5) and B (Co6–Co10, Table S2). We found that all of the Co^{II} complexes in **1** can be considered as the elongated from the ideal octahedral geometry which means that the average Co–N/O bond length along one direction is visibly longer than the average bond lengths in two other directions (Table S6). As the indicator of the elongation we calculated the relative difference [rd%] between the average bond length along the elongation axis in comparison with the average bond length within the perpendicular plane. We found the particularly large elongations in Co4 of clusters A (rd% = 2.71 %), and Co7 of clusters B (rd% = 2.57 %). More importantly, the average elongation for all the complexes is 1.57 % for clusters A, and 1.29 % for clusters B. It suggests that the overall anisotropy is presumably higher in seven-capped clusters A than in six-capped clusters B. This is with a good agreement with the overall structural anisotropy of the whole cluster cores which are elongated when compared with the ideal six-capped body centred cube topology for both types of clusters in **1** but the elongation was found to be visibly stronger in clusters A (*see* the structural studies in the main text, and Figures S4–S6). Interestingly, the arrangement of the elongation axes of the Co^{II} complexes are similar for clusters A and B, also in comparison to the elongation axes of the whole cluster cores which shows that the crucial difference between clusters A and B comes from the degree of deformation at both single complex and cluster levels.

Table S6. Analysis of the elongation of Co^{II} complexes in **1**

Complex	Bond lengths (1st direction, elongation) [Å]	Bond lengths (2nd direction) [Å]	Bond lengths (3rd direction) [Å]	Average bond length (elongation axis), BLE [Å]	Average bond length (other directions), BLO [Å]	Difference between average values of BLE and BLO [Å]	Relative difference between average values of BLE and BLO, rd%
Clusters A							
Co1	2.101 2.101	2.099 2.099	2.077 2.077	2.101	2.088	0.013	0.63
Co2	2.124 2.123	2.092 2.104	2.089 2.071	2.124	2.089	0.035	1.65
Co3	2.074 2.133	2.036 2.073	2.083 2.087	2.104	2.070	0.034	1.63
Co4	2.124 2.160	2.074 2.067	2.081 2.120	2.142	2.085	0.057	2.71
Co5	2.091 2.095	2.057 2.103	2.079 2.073	2.093	2.078	0.015	0.72
						weighted average rd%[a]	1.57
Clusters B							
Co6	2.114 2.114	2.088 2.088	2.071 2.071	2.114	2.080	0.035	1.66
Co7	2.170 2.106	2.067 2.077	2.105 2.089	2.138	2.085	0.053	2.56
Co8	2.123 2.126	2.123 2.075	2.091 2.059	2.124	2.087	0.037	1.79
Co9	2.097 2.093	2.045 2.044	2.072 2.098	2.095	2.065	0.030	1.46
Co10	2.088 2.096	2.113 2.052	2.088 2.078	2.092	2.083	0.009	0.44
						weighted average rd%[a]	1.29

[a]Weighted mean of rd% was calculated taking into account the amount of particular types of Co centers in the cluster.

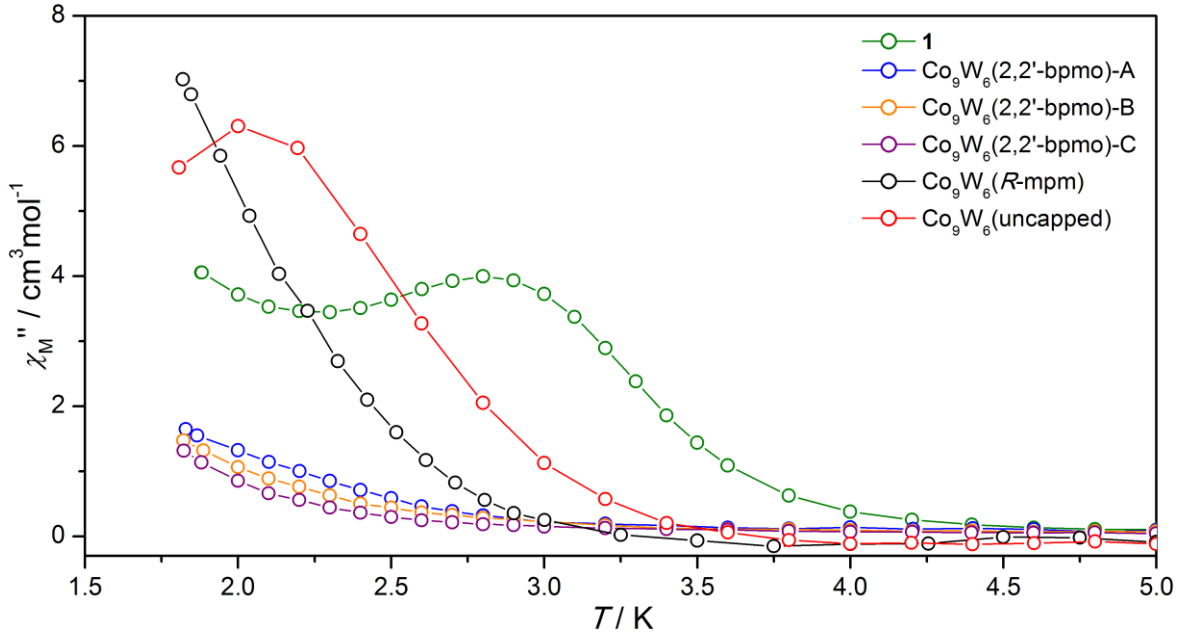

Figure S15. Comparison of the zero *dc* field χ_M''–*T* plots at the frequency of 1000 Hz for **1** (green) with the original purely solvated $\{Co^{II}_9W^{V}_6(MeOH)_{24}\}$ clusters (red),[S11] and other reported eightfold capped $\{Co^{II}_9W^{V}_6\}$ clusters with 2,2'-bpmo (2,2'-bipyridine N-oxide, three crystalline phases, A-C, blue, orange and purple colours, respectively),[S20] and *R*-mpm (*R*-methylpyridinemethanol, black).[S15] Note the significant shift of the signal towards higher temperatures for **1** when compared not only with all eightfold capped derivatives but also with the original uncapped cluster. As a result the thermal energy barrier was also significantly enhanced from the range of 10.1–22.3 K (Table S7) for the previously presented clusters to 30.0(8) K for **1**.

Table S7. Comparison of parameters of *ac* magnetic dynamics in **1** with other reported $[M(CN)_8]$-based Single-Molecule Magnets

compound	cluster core	$\Delta E/k_B$ (K)	τ_0 / s	ref.
1	**$\{Co_9W_6\}$**	**30.0(8)**	**$6(1)\cdot10^{-9}$**	this work
$\{Co^{II}[Co^{II}(MeOH)_3]_8[W^V(CN)_8]_6\}\cdot19H_2O$	$\{Co_9W_6\}$	22.3(0.3)[a]	$7.39\cdot10^{-11}$	S11
$\{Co^{II}[Co^{II}$(*R*-mpm)$(MeOH)]_8[W^V(CN)_8]\}\cdot14MeOH$ *R*-mpm = (*R*)-α-methyl-2-pyridinemethanol	$\{Co_9W_6\}$	19(4)	$4(2)\cdot10^{-9}$	S15
$\{Co^{II}[Co^{II}(MeOH)_3]_8[W^V(CN)_8]_6\}\cdot4,4'$-bpdo$\cdot MeOH\cdot H_2O$ 4,4'-bpdo = 4,4'-bipyridine N,N'-dioxide	$\{Co_9W_6\}$	10.3(5)	$4(1)\cdot10^{-9}$	S34
$\{Co^{II}[Co^{II}$(2,2'-bpmo)$(MeOH)]_6[Co^{II}$(2,2'-bpmo)$(MeCN)]_2$ $[W^V(CN)_8]\}\cdot8H_2O\cdot2MeCN\cdot2MeOH$ 2,2'-bpmo = 2,2'-bipyridine N-oxide	$\{Co_9W_6\}$	11(2)	$3.6(12)\cdot10^{-8}$	S20
$\{Co^{II}[Co^{II}$(2,2'-bpmo)$(MeOH)]_8[W^V(CN)_8]\}$ $\cdot H_2O\cdot8.5MeCN\cdot11.5MeOH$ 2,2'-bpmo = 2,2'-bipyridine N-oxide	$\{Co_9W_6\}$	10.1(11)	$3.3(9)\cdot10^{-8}$	S20
$\{Co^{II}[Co^{II}$(2,2'-bpmo)$(EtOH)]_8[W^V(CN)_8]\}$ $\cdot3H_2O\cdot5.5MeCN\cdot5EtOH$ 2,2'-bpmo = 2,2'-bipyridine N-oxide	$\{Co_9W_6\}$	10.7(14)	$1.7(6)\cdot10^{-8}$	S20
$\{[Ni^{II}_9$(tmphen)$_6(MeOH)_6(H_2O)_6][W^V(CN)_8]_6\}\cdot6$dmf tmphen = 3,4,7,8-tetramethyl-1,10-phenanthroline	$\{Ni_9W_6\}$	*ac* parameters not determined but the *M*(*H*) hysteresis loop detected below *T* = 1 K		S35
$\{[Cu^{II}$(L)$Tb^{III}(H_2O)_{3.5}]_4[Mo^{IV}(CN)_8]_2\}\cdot[Mo^{IV}(CN)_8]\cdot19H_2O$ L = N,N'-bis(3-methoxysalicylidene) ethylene diamine	$\{Cu_4Tb_4Mo_2\}$	19.25	$2.12\cdot10^{-6}$	S36
$\{[Ni^{II}(L^{Me2})Dy^{III}(H_2O)(L^{Me2})Ni^{II}]_2[W^V(CN)_8]_2\}\cdot10MeCN\cdot2H_2O$ L^{Me2} = compartmental Schiff base ligand	$\{Ni_4Dy_2W_2\}$	26.4	$6.0\cdot10^{-8}$	S37
$\{[Ni^{II}(L^{Me2})Tb^{III}(H_2O)(L^{Me2})Ni^{II}]_2[W^V(CN)_8]_2\}\cdot10MeCN\cdot2H_2O$ L^{Me2} = compartmental Schiff base ligand	$\{Ni_4Tb_2W_2\}$	23.0	$2.58\cdot10^{-7}$	S37
$\{[Cu^{II}$(L)$Tb^{III}(H_2O)_2]_2[W^{IV}(CN)_8]\}\cdot2\{[Ru^{II}(tpy)_2]X_2\}$ L = N,N'-bis(3-methoxysalicylidene) ethylene diamine tpy = 2,2';6',2"-terpyridine, X = NO_3^- or ClO_4^-	$\{Cu_2Tb_2W_2\}$	16.83 (with H_{dc} of 1600 Oe)	$3.93\cdot10^{-8}$	S38
$\{[Cu^{II}$(L)$Tb^{III}(H_2O)_2]_2[Mo^{IV}(CN)_8]\}\cdot2\{[Ru^{II}(tpy)_2]X_2\}$ L = N,N'-bis(3-methoxysalicylidene) ethylene diamine tpy = 2,2';6',2"-terpyridine, X = NO_3^- or ClO_4^-	$\{Cu_2Tb_2Mo_2\}$	*ac* parameters not determined but the *M*(*H*) hysteresis loop detected at *T* = 0.03 K		S38
$\{[Ni^{II}(L^{N3O2Ph})][Ni^{II}(L^{N3O2Ph})(H_2O)]_2[W^V(CN)_8]_2\}\cdot2MeCN\cdot12H_2O$ L^{N3O2Ph} = pentadentate pyridine-based ligand	$\{Ni_3W_2\}$	30	$1.6\cdot10^{-9}$	S39
$\{[Ni^{II}(L^{Me2})(H_2O)Tb^{III}(dmf)_{2.5}(H_2O)_{1.5}][W^V(CN)_8]\}\cdot H_2O\cdot0.5$dmf L^{Me2} = compartmental Schiff base ligand	{NiTbW}	15.3	$4.5\cdot10^{-7}$	S40

[a]In the literature (ref. S11) it is possible to find the energy barrier of 27.79 K for the slow magnetic relaxation in purely solvated $\{Co^{II}[Co^{II}(MeOH)_3]_8[W^V(CN)_8]_6\}\cdot19H_2O$ but it was only roughly estimated from the temperature dependence of out-of-plane magnetic susceptibility. We performed the more precise analysis of *ac* dynamics for this reference material, and the energy barrier of 22.3(0.3) K was found (unpublished results).

References to Supporting Information

(S1) A. Samotus, *Pol. J. Chem*., 1973, **47**, 653.

(S2) D. Matoga, J. Szklarzewicz and M. Mikuriya, *Inorg. Chem*., 2006, **45**, 7100.

(S3) S. Chorazy, R. Podgajny, W. Nogaś, W. Nitek, M. Kozieł, M. Rams, E. Juszyńska-Gałązka, J. Żukrowski, C. Kapusta, K. Nakabayashi, T. Fujimoto, S. Ohkoshi and B. Sieklucka, *Chem. Commun.*, 2014, **50**, 3484.

(S4) A. Vinciguerra, P. G. Simpson, Y. Kakuti and J. V. Quagliano, *Inorg. Chem*., 1963, **2**, 286.

(S5) G. M. Sheldrick, *Acta Crystallogr.*, 2008, **A64**, 112.

(S6) L. J. Farrugia, *J. Appl. Crystallogr.*, 1999, **32**, 837.

(S7) C. F. Macrae, I. J. Bruno, J. A. Chisholm, P. R. Edgington, P. McCabe, E. Pidcock, L. Rodriguez-Monge, R. Taylor, J. van der Streek and P. A. Wood, *J. Appl. Crystallogr.*, 2008, **41**, 466.

(S8) G. A. Bain and J. F. Berry, *J. Chem. Educ.*, 2008, **85**, 532.

(S9) M. Llunell, D. Casanova, J. Cirera, J. Bofill, P. Alemany, S. Alvarez, M. Pinsky and D. Avnir, *SHAPE v. 2.1. Program for the Calculation of Continuous Shape Measures of Polygonal and Polyhedral Molecular Fragments*, University of Barcelona: Barcelona, Spain, 2013.

(S10) D. Casanova, J. Cirera, M. Llunell, P. Alemany, D. Avnir and S. Alvarez, *J. Am. Chem. Soc.*, 2004, **126**, 1755.

(S11) Y. Song, P. Zhang, X.-M. Ren, X.-F. Shen, Y.-Z. Li and X.-Z. You, *J. Am. Chem. Soc*., 2005, **127**, 3708.

(S12) H. Isci and W. Roy Mason, *Inorg. Chim. Acta*, 2004, **357**, 4065.

(S13) S. Ohkoshi, Y. Hamada, T. Matsuda, Y. Tsunobuchi and H. Tokoro, *Chem. Mater*., 2008, **20**, 3048.

(S14) K. Nakabayashi, S. Chorazy, D. Takahashi, T. Kinoshita, B. Sieklucka and S. Ohkoshi, *Cryst. Growth Des.*, 2014, **14**, 6093.

(S15) S. Chorazy, M. Reczyński, R. Podgajny, W. Nogaś, S. Buda, M. Rams, W. Nitek, B. Nowicka, J. Mlynarski, S. Ohkoshi and B. Sieklucka, *Cryst. Growth Des*., 2015, **15**, 3573.

(S16) B. Papankova, R. Boca, L. Dlhan, I. Nemec, J. Titis, I. Svoboda and H. Fuess, *Inorg. Chim. Acta*, 2010, **363**, 147.

(S17) S. Chorazy, K. Nakabayashi, K. Imoto, J. Mlynarski, B. Sieklucka and S. Ohkoshi, *J. Am. Chem. Soc.*, 2012, **134**, 16151.

(S18) A. Mondal, L.-M. Chamoreau, Y. Li , Y. Journaux, M. Seuleiman and R. Lescouëzec, *Chem. Eur. J.*, 2013, **19**, 7682.

(S19) S. Chorazy, R. Podgajny, W.Nogaś, S. Buda, W. Nitek, J. Mlynarski, M. Rams, M. Kozieł, E. Juszyńska Gałązka, V. Vieru, L. F. Chibotaru and B. Sieklucka, *Inorg. Chem*., 2015, **54**, 5784.

(S20) S. Chorazy, A. Hoczek, M. Kubicki, H. Tokoro, S. Ohkoshi and B. Sieklucka, *CrystEngComm*, 2016, doi: 10.1039/C5CE02064F.

(S21) F. Lloret, M. Julve, J. Cano, R. Ruiz-Garcia and E. Pardo, *Inorg. Chim. Acta*, 2008, **361**, 3432.

(S22) Z. J. Zhong, H. Seino, Y. Mizobe, M. Hidai, A. Fujishima, S. Ohkoshi and K. Hashimoto, *J. Am. Chem. Soc*., 2000, **122**, 2952.

(S23) F. Bonadio, M. Gross, H. Stoeckli-Evans and S. Decurtins, *Inorg. Chem*., 2002, **41**, 5891.

(S24) Y. Song, P. Zhang, X.-M. Ren, X.-F. Shen, Y.-Z. Li and X.-Z. You, *J. Am. Chem. Soc*., 2005, **127**, 3708.

(S25) D. E. Freedman, M. V. Bennett and J. R. Long, *Dalton Trans*., 2006, 2829.

(S26) Z. Zhang, Y. Liu, R.-M. Wei, Z.-H. Sheng, P. Wang and Y. Song, *Inorg. Chem*. 2015, **54**, 11049.

(S27) M. Murrie, *Chem. Soc. Rev*., 2010, **39**, 1986.

(S28) N. I. Neuman, E. Winkler, O. Pena, M. C. G. Passeggi, A. C. Rizzi and C. D. Brondino, *Inorg. Chem*., 2014, **53**, 2535.

(S29) J. Vallejo, F. R. Fortea-Perez, E. Pardo, S. Benmansour, I. Castro, J. Krzystek, D. Armentano and J. Cano, *Chem. Sci*., 2016, doi: 10.10139/C5SC04461H.

(S30) S. Chorazy, R. Podgajny, W. Nitek, M. Rams, S. Ohkoshi and B. Sieklucka, *Cryst. Growth Des*., 2013, **13**, 3036.

(S31) B. Gillon, J. Larionova, E. Ruiz, Q. Nau, A. Goujon, F. Bonadio and S. Decurtins, *Inorg. Chim. Acta*, 2008, **361**, 3609.

(S32) Y.-Q. Zhang and C.-L. Luo, *Dalton Trans*., 2008, 4575.

(S33) Y.-Q. Zhang and C.-L. Luo, *Inorg. Chem*., 2009, **48**, 10486.

(S34) S. Chorazy, R. Podgajny, W. Nitek, M. Rams, S. Ohkoshi and B. Sieklucka, *Cryst. Growth Des*., 2013, **13**, 3036.

(S35) M. G. Hilfiger, H. Zhao, A. Prosvirin, W. Wernsdorfer and K. R. Dunbar, *Dalton Trans*., 2009, 5155.

(S36) J. Long, L.-M. Chamoreau and V. Marvaud, *Dalton Trans*., 2010, **39**, 2188.

(S37) S. Dhers, J.-P. Costes, P. Guionneau, C. Paulsen, L. Vendier and J.-P. Sutter, *Chem. Commun*., 2015, **51**,7875.

(S38) N. Bridonneau, L.-M. Chamoreau, P. P. Laine, W. Wernsdorfer and V. Marvaud, *Chem. Commun*., 2013, **49**, 9746.

(S39) N. Gogoi, M. Thlijeni, C. Duhayon and J.-P. Sutter, *Inorg. Chem*., 2013, **52**, 2283.

(S40) J.-P. Sutter, S. Dhers, R. Rajamani, S. Ramasesha, J.-P. Costes, C. Duhayon and L. Vendier, *Inorg. Chem*., 2009, **48**, 5820.